Basin Resonances in the Equatorial Indian Ocean

WEIQING HAN

Department of Atmospheric and Oceanic Sciences, University of Colorado, Boulder, Colorado

JULIAN P. MCCREARY

International Pacific Research Center, University of Hawaii at Manoa, Honolulu, Hawaii

YUKIO MASUMOTO

Research Institute for Global Change, Japan Agency for Marine–Earth Science and Technology, Yokohama, Japan

JÉRÔME VIALARD

IRD, LOCEAN, Paris, France

BENÉT DUNCAN

Department of Atmospheric and Oceanic Sciences, University of Colorado, Boulder, Colorado

(Manuscript received 24 September 2010, in final form 27 January 2011)

ABSTRACT

Previous studies have investigated how second-baroclinic-mode ($n = 2$) Kelvin and Rossby waves in the equatorial Indian Ocean (IO) interact to form basin resonances at the semiannual (180 day) and 90-day periods. This paper examines unresolved issues about these resonances, including the reason the 90-day resonance is concentrated in the eastern ocean, the time scale for their establishment, and the impact of complex basin geometry. A hierarchy of ocean models is used: an idealized one-dimensional (1D) model, a linear continuously stratified ocean model (LCSM), and an ocean general circulation model (OGCM) forced by Quick Scatterometer (QuikSCAT) wind during 2000–08. Results indicate that the eastern-basin concentration of the 90-day resonance happens because the westward-propagating Rossby wave is slower, and thus is damped more than the eastward-propagating Kelvin wave. Results also indicate that superposition with other baroclinic modes further enhances the eastern maximum and weakens sea level variability near the western boundary. Without resonance, although there is still significant power at 90 and 180 days, solutions have no spectral peaks at these periods. The key time scale for the establishment of all resonances is the time it takes a Kelvin wave to cross the basin and a first-meridional-mode ($\ell = 1$) Rossby wave to return; thus, even though the amplitude of the 90-day winds vary significantly, the 90-day resonance can be frequently excited in the real IO, as evidenced by satellite-observed and OGCM-simulated sea level. The presence of the Indian subcontinent enhances the influence of equatorial variability in the north IO, especially along the west coast of India. The Maldives Islands weaken the 180-day resonance amplitude but have little effect on the 90-day resonance, because they fall in its ''node'' region. Additionally, resonance at the 120-day period for the $n = 1$ mode is noted.

Corresponding author address: Weiqing Han, Department of Atmospheric and Oceanic Sciences, University of Colorado, UCB 311, Boulder, CO 80309.
E-mail: weiqing.han@colorado.edu

DOI: 10.1175/2011JPO4591.1

1. Introduction

a. Background

1) OBSERVATIONS

Observations from the equatorial Indian Ocean (IO) show particularly strong semiannual (180-day period) zonal surface currents, with eastward flow occurring during spring and fall (e.g., Wyrtki 1973; O'Brien and Hurlburt 1974; Knox 1976; Luyten and Roemmich 1982; McPhaden 1982; Gent et al. 1983; Molinari et al. 1990; Anderson and Carrington 1993; Donguy and Meyers 1995; Reppin et al. 1999). The semiannual current is much stronger than the annual one, whereas the semiannual zonal wind amplitude is comparable to the annual component (Han et al. 1999). At shorter time scales, strong spectral peaks of zonal surface current and sea level occur near the 90-day period, whereas the zonal wind peaks at 30–60 days (Han et al. 2001; Han 2005; Fu 2007); furthermore, the 90-day current and sea level signals are largest in the eastern equatorial IO, along the southern coast of Sumatra and Java, and in the Indonesian Seas (Qiu et al. 1999; Iskandar et al. 2005, 2006).

2) THEORY AND MODELING

Previous studies suggest that a possible explanation for the peak responses at both the 180- (Jensen 1993; Han et al. 1999) and 90-day (Han et al. 2001; Han 2005) periods is the establishment of basin resonance in the equatorial IO. Cane and Moore (1981) and Gent (1981) constructed low-frequency equatorial resonance modes in an idealized basin that consist of eastward-propagating Kelvin and westward-propagating, long-wavelength Rossby waves and that satisfy no-normal-flow boundary conditions at both eastern and western boundaries. The condition for resonance is

$$T = 4L/(mc_n), \tag{1}$$

where T is the forcing period, L is the equatorial basin width, c_n is Kelvin wave speed of the nth baroclinic mode ($n = 1, 2, \ldots$), and $m = 1, 2, \ldots$ is a positive integer. When (1) is satisfied and the model is inviscid, the solution becomes infinite at the locations,

$$x_f = x_e - (\pi c_n/4\omega)(2m' + 1), \tag{2}$$

and $m' = 0, 1, 2, \ldots$ is an integer (see Cane and Moore 1981; Cane and Sarachik 1981). In the above, x_e is the eastern boundary location and $\omega = 2\pi/T$ is frequency. Setting L to be the approximate width of the IO at the equator and the second-baroclinic-mode ($n = 2$) speed to be $c_2 = 167$ cm s^{-1}, (1) is satisfied for $T \approx 180$ days when $m = 1$ and for $T \approx 90$ days when $m = 2$. Based on (2), zonal surface currents become singular at the center of the basin for $T = 180$ days, and in both the eastern and western basins for $T = 90$ days. When friction is added, the singularities at x_f become finite local maxima (Cane and Moore 1981; Cane and Sarachik 1981). This theoretical solution suggests that the equatorial IO may preferentially respond to 180- and 90-day wind forcing, producing peak responses at these periods due to resonant excitation of the $n = 2$ mode.

Numerical models also generate resonances that amplify the direct wind-forced response at the semiannual (Jensen 1993; Han et al. 1999; Yuan and Han 2006) and 90-day periods (Han et al. 2001; Han 2005). It has been shown that resonance exists in both linear and nonlinear versions of a hierarchy of intermediate ocean models (Jensen 1993; Han et al. 1999, 2001), in a linear continuously stratified model (LCSM), and in an ocean general circulation model (OGCM; Han 2005). This diversity suggests that neither nonlinearity nor the complexity of basin geometry (e.g., the Maldives Islands) are critical factors in the dynamics of equatorial IO resonance, although nonlinearity has been speculated to be a major impediment to the existence of low-frequency basin resonances in the world's oceans (Cane and Moore 1981; Gent 1981).

b. Present research

A number of issues about IO basin resonances remain unresolved. For one thing, although both observed and simulated semiannual surface currents obtain their maximum amplitudes near the central basin as theoretically predicted (Jensen 1993; Han et al. 1999; Fu 2007), the eastern maximum is much more apparent than the western one for the 90-day basin resonance (Figs. 1b,c,e,f; see also Han 2005; Fu 2007); causes for this east–west asymmetry are not known. For another, the time scale for the setup of basin resonances is unclear; this issue is important for the 90-day resonance, because the 90-day wind that forces it has significant seasonality and interannual variability. Finally, just how the complex basin geometry of the IO affects the basin resonances has not been systematically examined.

We use a hierarchy of ocean models to address these issues: namely, a conceptual, one-dimensional (1D) linear model that allows for analytical solutions; an LCSM that allows solutions to be separated into contributions from individual baroclinic modes; and an OGCM—the Hybrid Coordinate Ocean Model (HYCOM)—forced by Quick Scatterometer (QuikSCAT) winds for the period of 2000–08, which demonstrates the frequent excitation of the 90-day basin resonance.

Our key results are the following: Horizontal mixing, vertical friction, and contributions from other baroclinic modes are the causes for the eastern-basin concentration

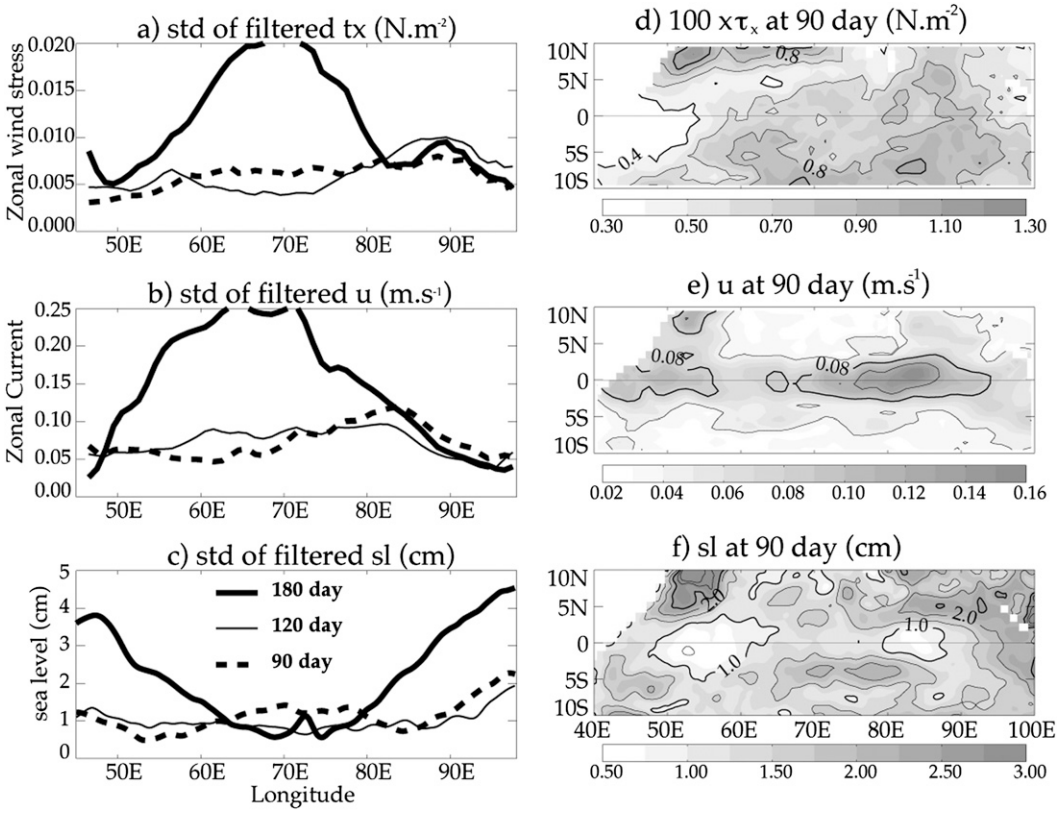

FIG. 1. (a) Standard deviation (STD) of observed zonal wind stress along the IO equator (2.5°N–2.5°S average) for 180- (thick solid), 90- (thick dashed), and 120-day (thin solid) periods based on a merged wind product from European Remote Sensing Satellite (ERS) and QuikSCAT scatterometers (Bentamy et al. 2002) from 1993 to 2008. Each period is extracted by filtering in Fourier domain and retaining Fourier coefficients between 0.9 and 1.1 times the central period, which is equivalent to 162–198 days bandpass filtering for 180-day resonance and 81–99 days for the 90-day resonance. Different filtering approaches (e.g., digital filtering, Hanning filter) have been used and they produce similar results. (b) As in (a), but for the Ocean Surface Current Analyses - Real time (OSCAR) zonal surface currents derived from observations for 1994–2008 (Bonjean and Lagerloef 2002). (c) As in (a), but from satellite-observed AVISO merged sea level anomalies (SLA; Ducet et al. 2000) for 1993–2008. Also shown are the STD maps for the observed 90-day (d) zonal wind stress, (e) zonal surface current, and (f) SLA described above.

of the 90-day resonance. The time it takes a Kelvin wave to cross the basin and a first-meridional-mode ($\ell = 1$) Rossby wave to return is the key time scale for the setup of all basin resonances. As a result, the 90-day basin resonance can be frequently excited in the real IO. The equatorial zonal surface currents associated with the basin resonances exhibit westward phase propagation at a speed faster than that of $\ell = 1$ Rossby wave because of the superposition of boundary-reflected Kelvin and Rossby waves. Finally, the existence of the Indian subcontinent and Sri Lanka enhances the impact of equatorial resonances in the northern IO, especially along the west coast of India.

2. Models and experiments

Although the 1D model is new, both the LCSM and HYCOM have been applied to various oceanic studies. Therefore, here we discuss the 1D model in detail but only describe aspects of the LCSM and HYCOM that are essential for this study.

a. The 1D model

Given the crucial roles played by the equatorial Kelvin and $\ell = 1$ Rossby waves in causing the equatorial IO basin resonances (e.g., Jensen 1993; Han et al. 1999; Han 2005), here we report solutions to a conceptual 1D model, which consists only of an eastward-propagating Kelvin wave and a westward-propagating, long-wavelength, $\ell = 1$ Rossby wave. (Essentially, the model can be viewed as a truncation of the LCSM that retains only the aforementioned waves for a single baroclinic mode.)

The model consists of the single equation,

$$(\partial_{t'} + c\partial_x)\left(\partial_{t'} - \frac{c}{3}\partial_x\right)q = F_0 X(x) e^{-i\omega t}, \qquad (3)$$

where $\partial_{t'} = \partial t + \gamma$, γ is a damping coefficient, and $F_0X(x)e^{-i\omega t}$ is a forcing at frequency ω with a spatial structure $X(x)$ and amplitude F_0. We assume the ocean basin is located in the range $0 \le x \le L$ and look for solutions to (3) that satisfy the boundary conditions,

$$q = 0 \quad \text{at} \quad x = 0, L, \tag{4}$$

so that q is analogous to zonal current. There are two free waves in (3): one that propagates eastward at speed c corresponding to an equatorial Kelvin wave and another that propagates westward at speed $c/3$ representing the $\ell = 1$, long-wavelength Rossby wave (e.g., Gill 1982). Because the equation is 1D along the equator, energy does not leak to higher latitudes. In an inviscid ocean, wave energy that impinges onto the western or eastern boundary has to be reflected back into the ocean interior.

Because the system is linear, q must also oscillate at frequency ω and so have the form

$$q(x,t) = \tilde{q}(x)e^{-i\omega t}. \tag{5}$$

Then, (3) can be rewritten as

$$(\partial_x - ik_K)(\partial_x + ik_R)\tilde{q} = -\frac{3}{c^2}F_0X(x), \tag{6}$$

where

$$k_K = \omega'/c, \quad k_R = -3\omega'/c = -3k_K, \quad \text{and} \quad \omega' = \omega + i\gamma. \tag{7}$$

For a general wind structure $X(x)$, a particular solution $\tilde{q}_p$ to (6) can be found using the method of Fourier transforms. The resulting solution is

$$\tilde{q}_p = -\frac{3}{4}\frac{F_0}{\sigma' c}\, i\left[e^{ik_Rx}\int_L^x e^{-ik_Rx'}X(x')\,dx' - e^{ik_Kx}\int_0^x e^{-ik_Kx'}X(x')\,dx'\right]. \tag{8}$$

The general solution is

$$q = [\tilde{q}_p + Ae^{ik_Kx} + Be^{ik_R(x-L)}]e^{-i\omega t}, \tag{9}$$

and to complete the solution we choose A and B to satisfy boundary conditions (4). Their values are

$$A = \frac{e^{ik_RL}\tilde{q}_p(0) - \tilde{q}_p(L)}{e^{ik_KL} - e^{ik_RL}} \quad \text{and}$$
$$B = -\tilde{q}_p(L) - Ae^{ik_KL}. \tag{10}$$

In the above, $\tilde{q}_p$ represents the sum of Kelvin and Rossby waves directly driven by winds in an infinite basin without boundaries [Eq. (8)]; Ae^{ik_Kx} denotes the Kelvin wave reflected from the western boundary; and $Be^{ik_R(x-L)}$ is the Rossby wave reflected from the eastern boundary [Eq. (9)].

Resonance occurs when the denominator of (10) becomes small so that the contribution of the boundary waves is large. Neglecting damping, the denominator vanishes ($e^{ik_KL} - e^{ik_RL} = 0$) when Eq. (1) is satisfied. Furthermore, it is straightforward to show that the resonant peaks of (9) occur at the longitudes x_f given by (2). Thus, our simple 1D model is able to capture basic properties of the more complex 2D model of Cane and Moore (1981). This similarity is noteworthy: It suggests that resonance in the 2D model is dominated by contributions from the Kelvin wave and the $\ell = 1$ Rossby wave, even though the solution sums an infinite number of meridional-mode Rossby waves.

To further demonstrate the effect of basin resonance, we find a solution in a semi-infinite basin without a western boundary. It is

$$q_{\text{nw}} = [\tilde{q}_p - \tilde{q}_p(L)e^{ik_R(x-L)}]e^{-i\omega t}, \tag{11}$$

where $\tilde{q}_p$ is again given by (8).

A suite of solutions is found using three different forcing structures $X(x)$ and varying friction. The three forcing structures are illustrated below in the top panel of Fig. 2a. They are (i) basinwide constant, representing the observed basinwide power of 180- and 90-day zonal wind stress (Figs. 1a,d); (ii) midbasin top hat, resembling the large amplitude of 180-day wind in the central basin (Fig. 1a); and (iii) east-enhanced top hat, mimicking the eastern-basin-enhanced strength of 90-day wind (Figs. 1a,d). The solutions are summarized in Table 1.

b. The LCSM

The LCSM is described in detail in McCreary (1980, 1981), and it has been applied to various IO studies, including equatorial resonance (Shankar et al. 1996; McCreary et al. 1996; Miyama et al. 2003; Han et al. 2004; Han 2005). The equations of motion are linearized about a state of rest with a realistic background stratification $\rho_b(z)$ and Väisälä frequency $N^2 = -(g/\rho_0)\rho_{bz}$, where $g = 980$ cm s^{-2} and ρ_0 is the mean density of seawater. In addition, vertical mixing coefficients have the depth-dependent form A/N^2, where A is a constant and the ocean bottom is assumed flat. With these restrictions, solutions can be represented as expansions in the vertical normal modes of the system, and the total solution is the sum of all the modes. The characteristic speeds c_n for the first four baroclinic modes, estimated

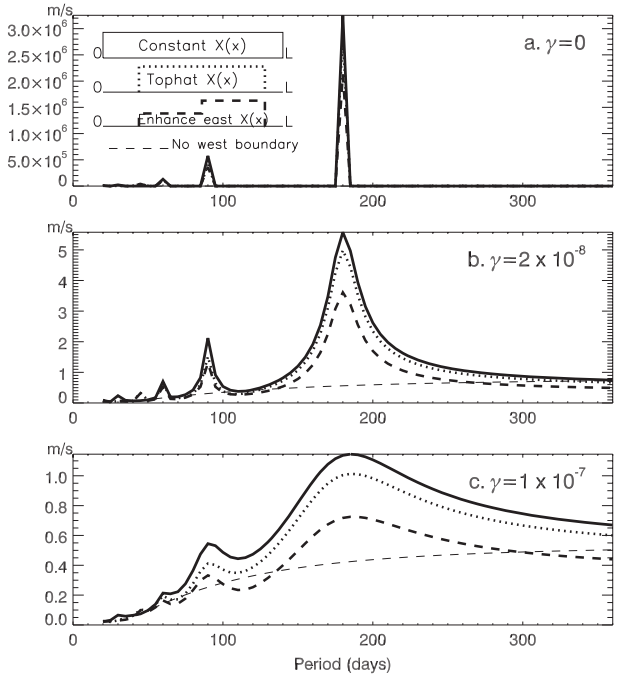

FIG. 2. The maximum amplitude of q [Eq. (9)], $|q|_{\max} = \max(\sqrt{\mathrm{Re}^2 + \mathrm{Im}^2})$, across the 1D basin at each of the periods of $T = 20, 25, \ldots, 360$ days when the structure of zonal wind forcing is constant across the basin (solid curves), a top-hat function at $0.2L$–$0.9L$ of the basin (dotted), and a top hat with eastern-basin enhancement (thick dashed); the maximum amplitude of q_{nw}, the solution in a semi-infinite basin without western boundary [Eq. (11)] with the eastern-basin-enhanced top-hat wind forcing, is also shown (thin dashed). Here, q represents zonal surface current [see Eqs. (3) and (4)], and Re and Im are the real and imaginary parts of q. (a) Inviscid ocean ($\gamma = 0$), solutions to 1DExp1a,b,c (Table 1) (zonal structures of the three forcing winds are also shown); (b) $\gamma = 2 \times 10^{-8}$ s^{-1}, solutions to 1DExp2a,b,c; and (c) $\gamma = 10^{-7}$ s^{-1}, solutions to 1DExp3a,b,c. The forcing winds are white noises and thus have no preferred periods (see Table 1).

from a mean $\rho_b(z)$ based on IO density observations (see Moore and McCreary 1990), are $c_1 = 264$ cm s^{-1}, $c_2 = 167$ cm s^{-1}, $c_3 = 105$ cm s^{-1}, and $c_4 = 75$ cm s^{-1}. These values are close to the characteristic speeds estimated by M. Nagura and M. J. McPhaden (2010, personal communication). In the experiment with the Maldives, the islands are represented by rectangular boxes along 73°–74°E at 0°–1°N and 2°–6°N. No-slip conditions are used along continental and island boundaries; the southern boundary is open, and zero-gradient boundary conditions are applied. A hierarchy of experiments is performed with different wind forcing, friction, and basin geometries. They are summarized in Table 2.

c. The OGCM–HYCOM

The HYCOM is documented in detail in Bleck (2002) and Halliwell (1998, 2004). Here, it is configured to apply to the tropical IO north of 30°S, with a horizontal resolution of 0.5° × 0.5°, a realistic bottom topography, and 18 sigma layers, as in Han (2005). The nonlocal K-profile parameterization (KPP) is used for the boundary layer mixing scheme (Large et al. 1994, 1997). Solar shortwave radiation penetration is included with Jerlov water-type IA (Jerlov 1976). Along continental boundaries, no-slip boundary conditions are applied. Near the southern boundary and the Indonesian Throughflow region, sponge layers of 5° are applied to relax the model temperature and salinity to the Levitus and Boyer (1994) and Levitus et al. (1994) climatologies.

HYCOM is spun up from a state of rest for 30 yr using the 2000–08 monthly climatological fields derived from QuikSCAT winds (Tang and Liu 1996), net longwave and shortwave radiative fluxes from the International Satellite Cloud Climatology Project flux data (ISCCP-FD; Zhang et al. 2004), National Centers for Environmental Prediction (NCEP) air temperature and specific humidity (Kalnay et al. 1996), and Climate Prediction Center (CPC) Merged Analysis of Precipitation (CMAP) pentad data (Xie and Arkin 1996). HYCOM is then integrated forward in time, forced by the 3-day mean values of the above forcing fields for the period of 2000–08. Results for years 2001–08 are analyzed.

3. Results

In this section, we first identify the prominent basin resonances present in our solutions and report their spatial structures. Although our focus is on the 180- and 90-day resonances for the $n = 2$ mode, we also discuss the 120-day resonance for the $n = 1$ mode. Next, we explore causes for the eastern-basin concentration of the 90-day basin resonance, assess impacts of basin geometry, and investigate the time scale for establishing the resonances. Finally, we obtain realistic HYCOM solutions that indicate the frequent occurrence of the 90-day basin resonance in the real IO.

a. Basin-resonant structure and eastern-basin concentration

1) SOLUTIONS TO THE 1D MODEL

Figure 2 plots the maximum amplitude of q [see Eq. (9)], $|q|_{\max}$, across the 1D basin at each period from the 1D model experiments when $c = c_2 = 167$ cm s^{-1}, for the various values of γ and $X(x)$. When $\gamma = 0$ (Fig. 2a), basin resonances clearly exist at $T = 180$, 90, and 60 days, with amplitudes that weaken for smaller T. The amplitudes of the inviscid solutions (Fig. 2a) are very large. (They are not infinitely large, because periods are very close to but not precisely at the exact resonant periods.) As friction increases (Figs. 2b,c), the resonant peaks

TABLE 1. The suite of experiments performed using the 1D model for the $n = 2$ baroclinic mode $c_2 = 167$ cm s^{-1}. The experiments use different wind forcings and friction values in a zonal basin with $L = 6493$ km. Each experiment is forced by white noise of zonal wind stress at a series of periods. 1DExp1a is inviscid and forced by basinwide constant F_0 with $F = F_0 e^{-i\omega t}$, where $\omega = 2\pi/T$ and $T = 20, 25, \ldots$ 360 days, respectively. The spatial structure and amplitude of wind are the same for all periods, except that temporally they oscillate at different periods. 1DExp1b is the same as 1DExp1a, but the forcing has a top-hat structure confined to the region for $0.2L < x < 0.9L$ of the basin, where L is the equatorial IO basin width. 1DExp1c is the same as 1DExp1b, but the top-hat forcing is weakened by half in the region $0.2L < x < 55L$. 1DExp2a,b,c and 1DExp3a,b,c are the same as Exp1a,b,c, but for $\gamma = 2 \times 10^{-8}$ s^{-1} and $\gamma = 1 \times 10^{-7}$ s^{-1}, respectively.

Expt	Forcing zonal wind stress	Friction γ
1DExp1a,b,c	F_0 = constant; midbasin top hat; east-enhanced top hat	$\gamma = 0$
1DExp2a,b,c	Same as above	$\gamma = 2 \times 10^{-8}$
1DExp3a,b,c	Same as above	$\gamma = 1 \times 10^{-7}$

become weaker and broader. Differences among the solutions for different wind structures $X(x)$ are less striking; their amplitudes become sequentially weaker as $X(x)$ changes from a basinwide constant to a midbasin top hat and to an eastern-enhanced structure (solid, dotted, and thick dashed curves, respectively). Without a western boundary, solutions in a semi-infinite basin [q_{nw} of Eq. (11)] do not show peak responses at 180- and 90-day periods (thin dashed lines), although there is significant power at these periods when friction is added (Figs. 2b,c). Without friction, the amplitude of q_{nw} is too weak to be seen (Fig. 2a). These results clearly suggest that the observed selective responses of the equatorial IO to 180- and 90-day wind forcing result from basin resonances that require both eastern and western boundaries for their existence (cf. the thick and thin dashed curves).

Figures 3 and 4 illustrate the structures of the 180- and 90-day responses, plotting the total response (thick curves), the interior response (particular solution; thin curves), and the resonant Rossby and Kelvin wave response (dashed–dotted curves). In an inviscid ocean and regardless of the choice of $X(x)$, $|q|$ has one maximum in the central basin for $T = 180$ days (Figs. 3a–c) and two maxima, located in the western and eastern basins, for $T = 90$ days (Figs. 4a–c). The large amplitudes result entirely from the resonant response of reflected Kelvin and Rossby waves (cf. thick and dashed–dotted curves in Figs. 3a–c, 4a–c), with the interior response being so small that it cannot be seen. When friction is included, however, east–west asymmetry occurs at both the 180- and 90-day periods, especially the latter period (Figs. 3d–i, 4d–i). As friction increases, the asymmetry becomes more apparent for a given $X(x)$, the contribution from the boundary waves weakens (dashed–dotted curves), and hence the interior solution becomes increasingly important (thin solid lines) in the total response. Under the influence of friction, both the interior response and boundary reflections establish east–west

TABLE 2. The suite of LCSM experiments using different wind forcings, friction values, and basin geometries. As for the 1D model, each experiment is forced by τ^x white noise at a series of consecutive periods. The spatial structure and amplitudes of wind are the same at all periods. LMExp1 has a rectangular basin and no vertical friction ($A = 0$) and is forced by constant zonal wind stress structure in the entire basin for $T = 30, 33, \ldots, 390$ days, respectively. To ensure numerical stability, harmonic horizontal mixing is included in the model (section 2). LMExp2 is the same as LMExp1, but vertical friction with $A = 0.000\ 13$ cm^2 s^{-3} is included. LMExp3 is the same as LMExp2, but the forcing is confined to the latitude band 15°S–15°N zonal wind stress forcing. It is constant for 10°S–10°N and gradually reduces to zero at 15°S and 15°N using a cosine taper. LMExp4, LMExp5 , LMExp6, and LMExp7 are the same as LMExp3, but using a realistic eastern boundary, realistic eastern and western boundaries, a realistic IO basin without the Maldives, and a realistic IO basin with the Maldives. LMExp8 is the same as LMExp6, but τ^x is confined to the longitudinal band 60°E $< x <$ 100°E and gradually reduces to zero at 60° and 100°E using a cosine taper. Finally, the LM_CR is forced by 3-day mean QuikSCAT winds for 2000–08. It is restarted on 1 Jan 2000 from an already spun-up LM solution forced by 40-yr European Centre for Medium-Range Weather Forecasts (ECMWF) Re-Analysis (ERA-40) winds.

Expt	Forcing wind	Basin geometry	Friction
LMExp1	Basinwide constant τ^x	Rectangle	$A = 0$
LMExp2	Basinwide constant τ^x	Rectangle	$A = 0.000\ 13$
LMExp3	15°S–15°N τ^x	Rectangle	$A = 0.000\ 13$
LMExp4	15°S–15°N τ^x	Real east boundary	$A = 0.000\ 13$
LMExp5	15°S–15°N τ^x	Real east and west	$A = 0.000\ 13$
LMExp6	15°S–15°N τ^x	Real IO no Maldives	$A = 0.000\ 13$
LMExp7	15°S–15°N τ^x	Real IO and Maldives	$A = 0.000\ 13$
LMexp8	15°–15°N, 60°–100°E τ^x	Real IO no Maldives	$A = 0.000\ 13$
LM_CR	3-day mean QuikSCAT wind forcing, 2000–08	Real IO basin geometry	$A = 0.000\ 13$

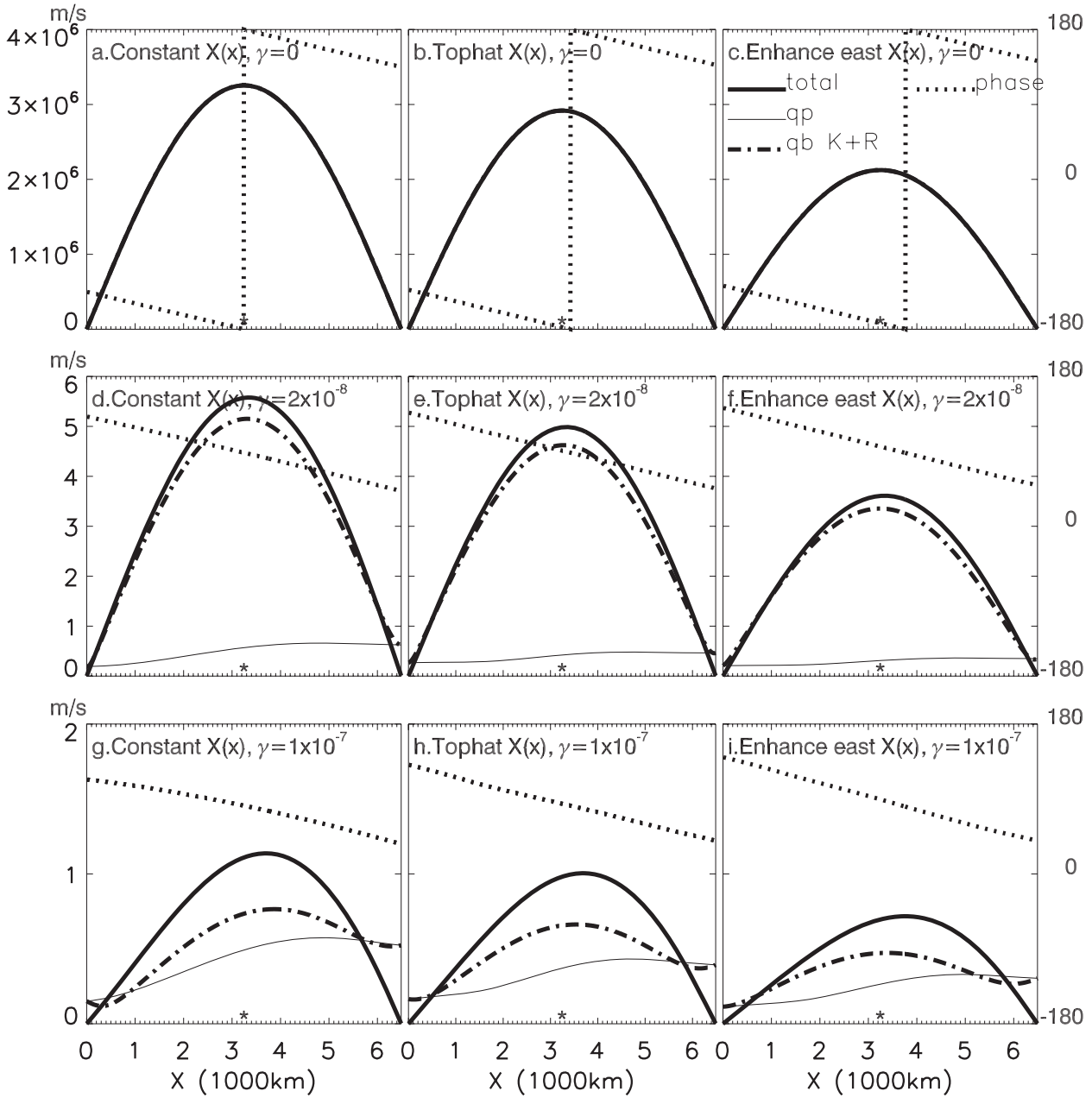

FIG. 3. Zonal structure of q amplitude, $|q| = \sqrt{\mathrm{Re}^2 + \mathrm{Im}^2}$, for the 180-day basin resonance (thick solid curves), which is the resonance solution of the second ($n = 2$) baroclinic mode when $m = 1$: (a) uniform forcing, (b) top-hat forcing at 0.2–0.9L of the basin, and (c) top hat with eastern-basin enhancement without friction ($\gamma = 0$). (d)–(f) As in (a)–(c), but for $\gamma = 2 \times 10^{-8}$ s^{-1}. (g)–(i) As in (a)–(c), but for $\gamma = 10^{-7}$ s^{-1}. In each panel, the amplitudes of interior particular solution (qp; thin solid lines), the sum of boundary Kelvin and Rossby waves (qb K+R; dashed–dotted lines) determined from Eqs. (8)–(10), and phase of q (dotted lines) are also plotted. Note that $|q|$ is shown for each solution, rather than q itself. Consequently, the sum of the amplitudes from the particular solution (thin solid) and from boundary Kelvin and Rossby waves (dashed–dotted) does not equal the amplitude of the total solution (thick solid). The asterisk near the bottom of each panel denotes the midbasin location.

asymmetry and thus both contribute to the enhanced response in the eastern basin. This asymmetry happens because the $\ell = 1$ Rossby wave propagates westward more slowly than the Kelvin wave propagates eastward ($c_R = -c_K/3$) and therefore is damped 3 times as much as it crosses the basin. Note that the enhanced eastern-basin wind does not significantly contribute to the asymmetry of the basin resonance. The 60-day basin

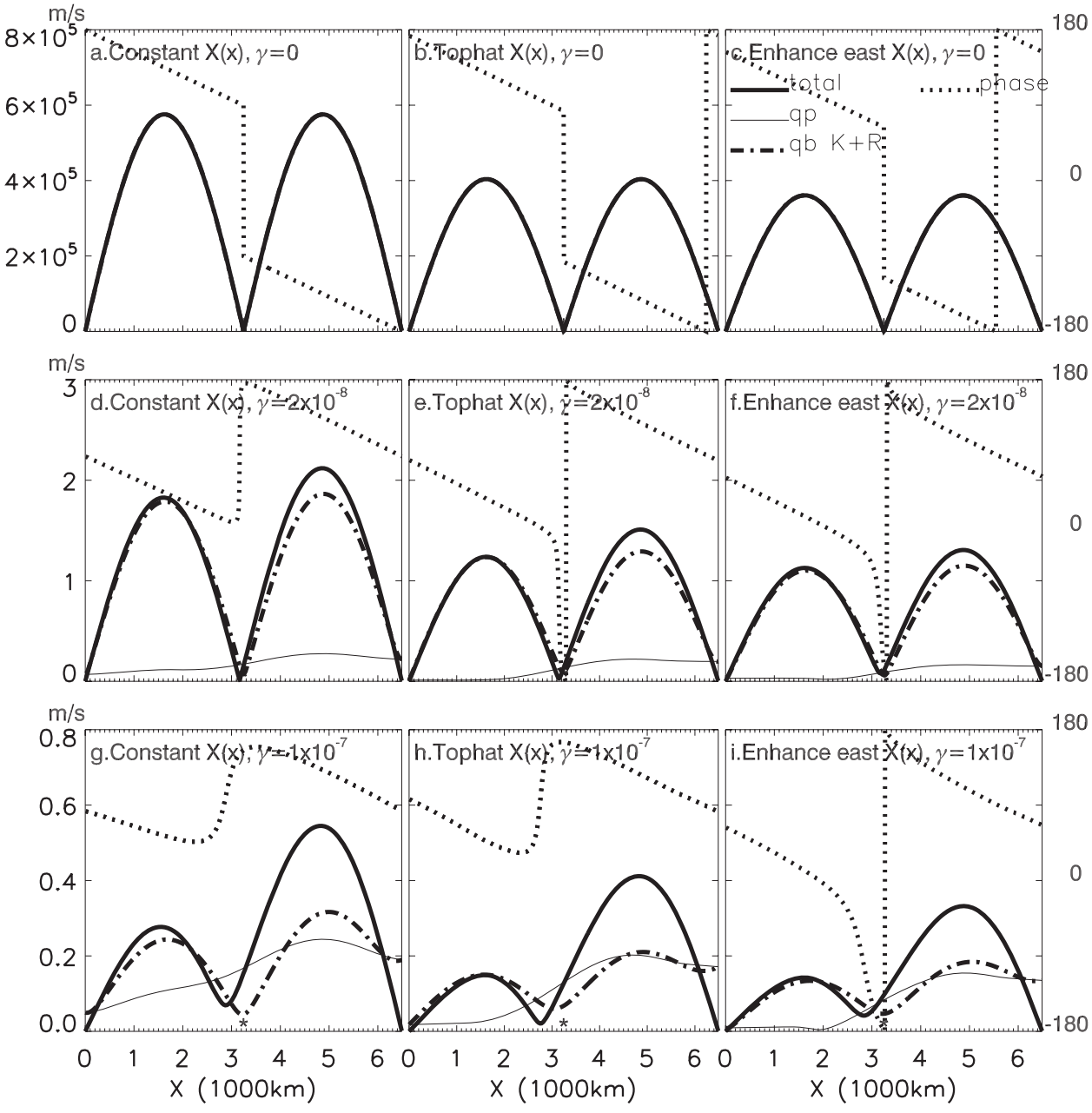

FIG. 4. As in Fig. 3, but for the 90-day basin resonance when $m = 2$.

resonance (not shown), which occurs when $m = 3$ in (1), is much weaker and hardly detectable when friction is large (Fig. 2).

Figures 3 and 4 also plot the phase of the total response (dotted curves). Interestingly, q exhibits westward phase propagation (phase increases to the west) at a speed faster than the $\ell = 1$ Rossby wave for both the 180- and 90-day basin resonances, consistent with the observations (Nagura and McPhaden 2010; M. Nagura and M. J. McPhaden 2010, personal communication). Our solutions suggest that this westward propagation of q results primarily from a superposition of boundary-reflected Kelvin and Rossby waves, with interior solution modifying the phase near its discontinuity regions and boundaries when friction is added (not shown). These results agree with previous studies, which suggest the importance of eastern-boundary-reflected Rossby waves in causing westward phase propagation (Fig. 5 of Han et al. 1999; Nagura and McPhaden 2010; M. Nagura and M. J. McPhaden 2010, personal communication).

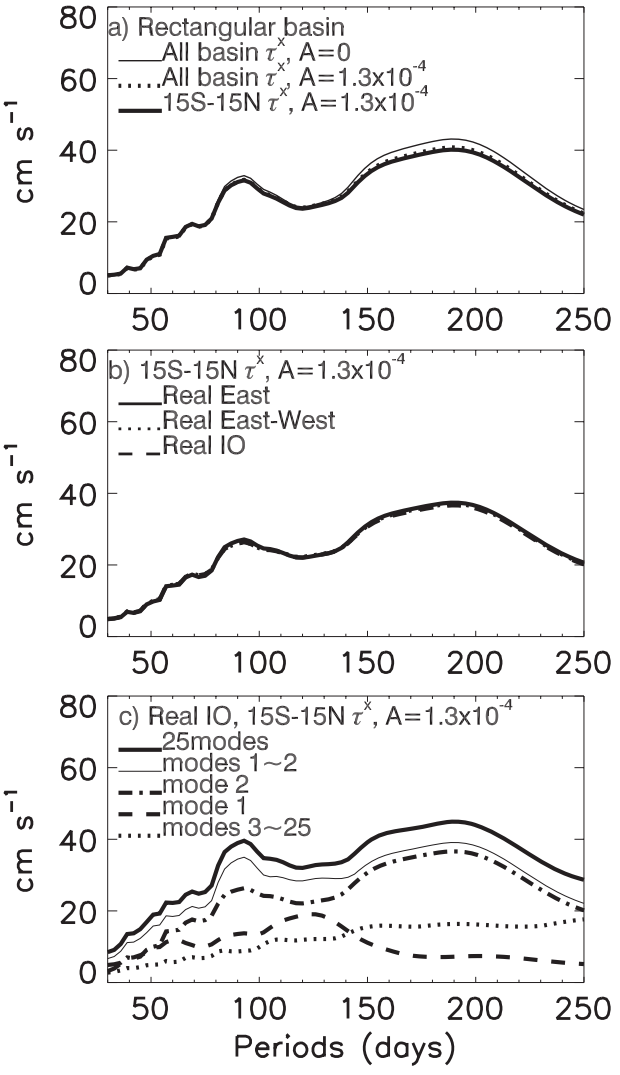

FIG. 5. (a) As in Fig. 2, but for the LCSM maximum amplitude of zonal surface current along the equator (2°S–2°N average), showing a series of LCSM experiments for the $n = 2$ mode, using varying wind and friction (see Table 2). (b) As in (a), but for varying basin geometry. (c) As in (a), but for realistic IO basin geometry, 15°S–15°N wind forcing and with friction, showing the sums of all modes (thick solid), modes 1 and 2 (thin solid), modes 3–25 (dotted), only mode 1 (dashed), and only mode 2 [dashed–dotted; same as the dashed line shown in (b)]. Results shown are from model year 5, when equilibrium is basically reached.

2) LCSM SOLUTIONS

The preceding resonances are also present in solutions of the LCSM for the $n = 2$ mode. To illustrate, Fig. 5 plots the maximum amplitude of the zonal surface current in solutions driven by the wind fields shown in Figs. 6a,b. For basinwide forcing in a rectangular basin (Fig. 5a), note that, even for the solution with no vertical mixing ($A = 0$), 180- and 90-day resonances both have finite amplitudes (thin solid line), a consequence of the LCSM including Laplacian horizontal mixing to ensure numerical stability and of the poleward radiation of coastal Kelvin waves along the eastern boundary (see the discussion of Fig. 9 below). By including vertical mixing ($A \neq 0$), the amplitudes are only slightly reduced (dotted line), because vertical mixing is weak for low-order modes. The maximum amplitudes of zonal surface currents also remain almost unchanged when the forcing wind is changed from basinwide to be confined from 15°S to 15°N (thick curve), indicating that the equatorial basin resonance is primarily forced by tropical winds. Consistent with the 1D solutions, the 60-day basin resonance is hardly detectable. When the basin geometry becomes progressively more realistic (Fig. 5b), current maxima on the equator essentially are unchanged. Realistic basin geometry, however, does cause north–south asymmetry, which will be discussed in section 3b.

The $n = 1$ mode also has a resonant character (Fig. 5c, dashed), with a clear resonance near 120 days for $m = 1$ in Eq. (1) and more weakly near 60 days for $m = 2$. These resonances also appear in the 1D model solutions forced by various wind structures when we choose $c_1 = 264$ cm s^{-1} (not shown). As for the $n = 2$ mode, the $n = 1$ curve is not sensitive to basin geometry and friction. The 120- and 60-day relative peaks that appear in the $n = 1$ mode solution, however, cannot be seen in the superposition of the $n = 1$ and $n = 2$ modes solutions (Fig. 5c, thin solid) or in the total solution (thick solid). This lack suggests that, if the forcing winds are white noise with no preferred frequency, the $n = 1$ mode resonance may not be identifiable in other models or the real ocean. (In contrast, the $n = 2$ mode resonances at both 90- and 180-day periods are visible; compare the dashed–dotted and solid lines.) On the other hand, if the forcing winds are especially strong at the 120- or 60-day periods, these $n = 1$ basin resonances may stand out. Note that higher-order baroclinic modes ($n \geq 3$; dotted) also contribute significantly to the amplitudes of the 180- and 90-day currents (see also Fig. 7). Indeed, the increasing trend of total current amplitude with the increase of period results largely from the higher-order modes, the response of which is primarily local and hence proportional to its forcing period T when $A = 0$ (see Han 2005). It is the basin resonances that account for the relative peaks of current amplitudes.

Figure 5 shows that the amplitude and structure of the equatorial basin resonances are primarily forced by tropical winds and influenced little by friction. Hereafter, then, we focus on solutions forced by the 15°S–15°N winds (Fig. 6b) with $A = 1.3 \times 10^{-4}$ cm^2 s^{-3}. Corresponding experiments forced by winds confined to the central-eastern basin [Fig. 6c; linear model experiment 8 (LMExp8)] differ primarily in that they have weaker amplitudes.

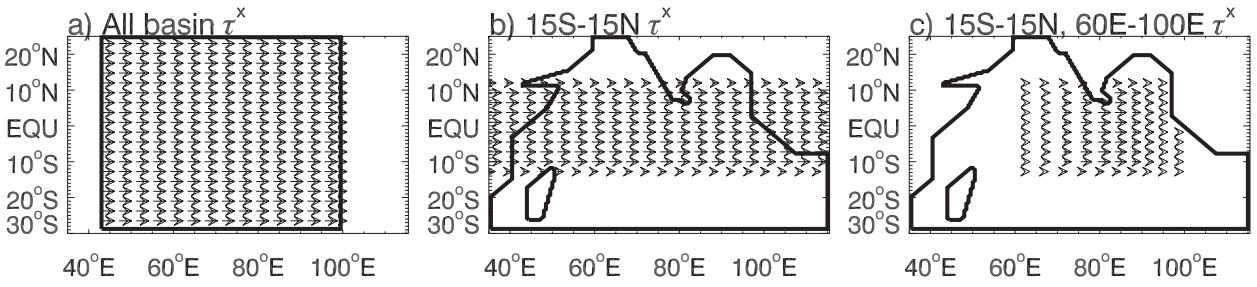

FIG. 6. Spatial structures of zonal wind stresses τ^x that oscillate at various periods and are used to force the LCSM (LMExp1–LMExp8; Table 2). (a) Basinwide constant structure with an amplitude of 0.15 dyn cm^{-2}. (b) Forcing τ^x is confined to 15°S–15°N, with a constant amplitude of 0.15 dyn cm^{-2} within 10°S–10°N, and decreasing to zero at 15°S and 15°N using a cosine taper. (c) As in (b), but τ^x also decreases zonally using a cosine taper from 80°E to zero at 60°E in the west and at 100°E in the east.

Consistent with the 1D model solution, zonal surface currents from the LCSM forced by periodic zonal wind stress with a spatial structure of Fig. 6b (Figs. 7a–c) have a single maximum in the central equatorial ocean for the 180-day resonance (Fig. 7d), have two relative maxima for the 90-day resonance (Fig. 7e), and exhibit westward phase propagation. The 120-day resonance attains a maximum near the central basin (Fig. 7i). As expected, larger amplitudes occur for the $n = 2$ mode at 180- and 90-day periods than at 120-day period, with the $n = 1$ mode also contributing significantly to the 90-day current (cf. Figs. 7d–f). In contrast, the largest amplitude occurs for the $n = 1$ mode at 120-day period, but the $n = 1$ and $n = 2$ modes contribute almost equally to the 120-day current (cf. Figs. 7g–i).

Figures 8 and 9 illustrate the spatial structures of surface currents (left panels) and sea level (right panels) for the 180- and 90-day resonances, respectively, showing the response at a time when the zonal surface current attains its maximum amplitude. (The structures for the 120-day basin resonance are not shown because they are similar to those for the 180-day one.) For the 180-day resonance, the surface current obtains its maximum in the central basin, regardless of the basin geometry (Figs. 8a–d). The sea level structure is more complex, with relative maxima occurring near both the eastern and western boundaries and relative minima occurring north and south of the equator in the central and eastern basin where u is strong (Figs. 8e–h). These structures are consistent with the observed 180-day zonal surface current and sea level structures along the equator (thick solid lines of Figs. 1b,c). The equatorial currents and sea level structure are linked by $u \approx -(g/\beta)h_{yy}$, where $\beta = f_y$ and h is sea level, the equatorial expression of the geostrophic relation. Thus, at locations where equatorial u obtains its maximum, so does $-h_{yy}$, (dotted lines in Figs. 8c,g).

As in the 1D model, the 90-day resonance has two relative maxima for zonal surface currents along the equator in the eastern and western basins (Figs. 9a–d). In the two regions of zonal-current maxima, $-h_{yy}$ obtains large amplitudes (Figs. 9c,g), and the eastern one is larger than the western one, as for the currents. These structures resemble those of the observed zonal surface current and sea level near the 90-day periods (Figs. 1e,f). This east–west asymmetry of the 90-day basin resonance results largely from horizontal mixing and, to a lesser degree, friction in the LCSM, as demonstrated by LMExp1 and LMExp2 (not shown). Figures 8 and 9 also show that, when the basin is extended from one to two dimensions, part of the energy leaks to higher latitudes along the eastern boundary of the basin via coastal Kelvin waves, where it is damped by horizontal mixing. It is this process that ensures the resonant solutions remain finite even when vertical mixing is zero ($A = 0$).

The superposition of all baroclinic modes, especially the $n = 1$ and $n = 2$ modes, further enhances the eastern concentration of maximum current and obscures the secondary western maximum of the 90-day basin resonance (cf. Figs. 10c,d with Figs. 9c,g). Similarly, superposition of the first two baroclinic modes reduces the secondary maximum of sea level in the western equatorial basin for the 180-day basin resonance (cf. Figs. 10a,b with Figs. 8c,g). These properties suggest that, in the real ocean, the superposition of all modes can obscure basin-resonance structures. Consequently, the 90- or 180-day currents and sea level obtained from observations or OGCM solutions by bandpass filtering represent the total effects of all baroclinic modes at the corresponding period and may not represent pure basin-resonant structures (cf. Figs. 1e,f with Figs. 9c,g), even though they qualitatively agree because of the dominance of basin resonances.

b. *Effects of basin geometry and the Maldives*

As shown in Fig. 5b, equatorial current maxima are essentially unchanged, when the basin geometry becomes

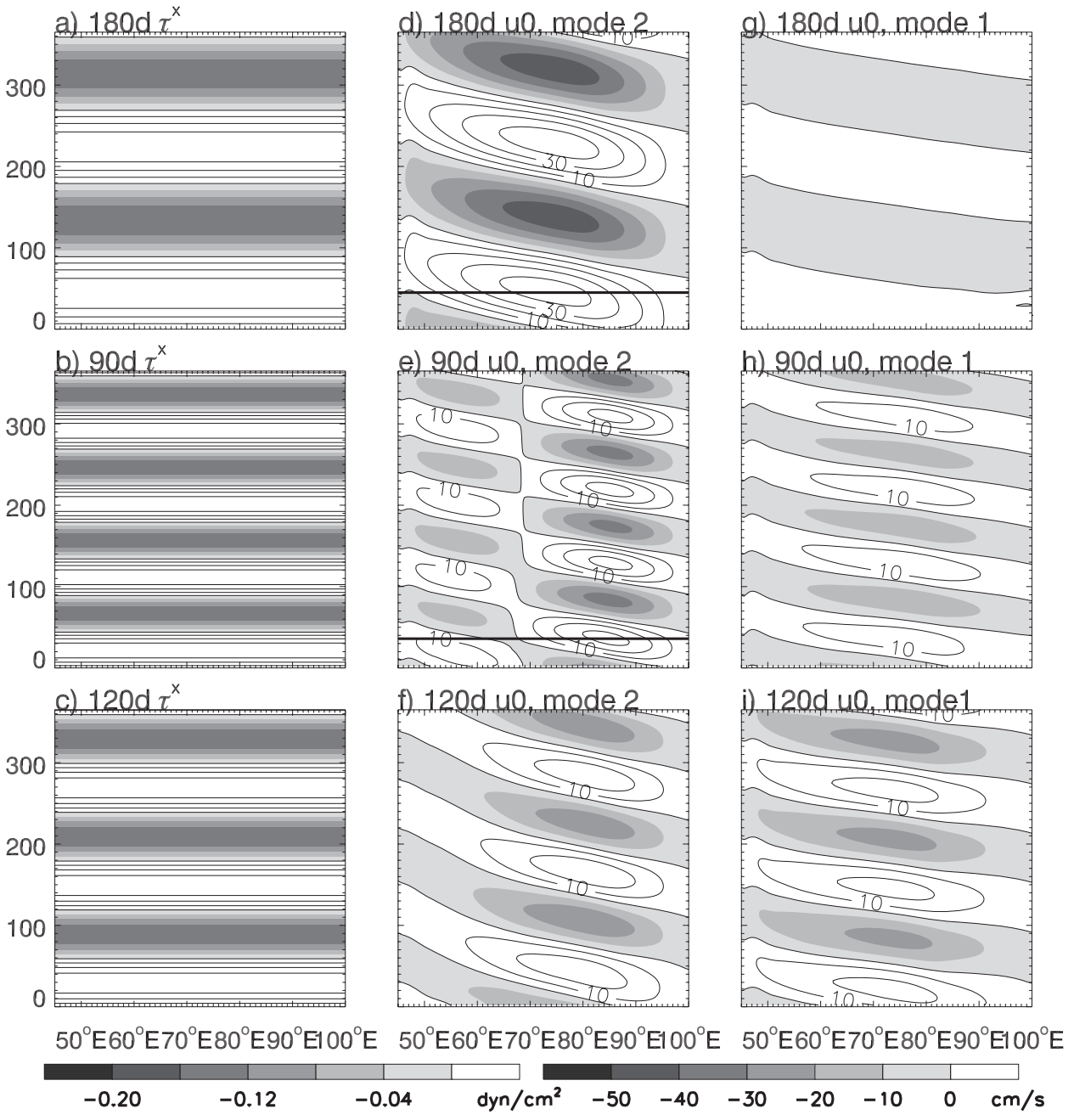

FIG. 7. (a)–(c) Longitude–time plots of zonal wind stress τ^x (dyn cm^{-2}) from Fig. 6b averaged for 2°S–2°N along the IO equator at T = 180, 90, and 120 days, respectively. (d)–(f) As in (a)–(c), but showing zonal surface current u_0 (cm s^{-1}) from the $n = 2$ mode solution with a realistic IO basin, LMEXP6. (g)–(i) As in (d)–(f), but for $n = 1$ mode. The two horizontal black lines in (d) and (e) mark the times during year 5 when the current and sea level solutions are shown in Figs. 8 and 9. Positive values are contoured and negative values are shaded, with an interval of 0.04 dyn cm^{-2} for wind stress and 10 cm s^{-1} for current.

progressively more realistic, by including a realistic eastern boundary (solid curve), both eastern and western boundaries (dotted curve), and the Indian subcontinent together with Sri Lanka and Madagascar (dashed curve). Furthermore, Figs. 8 and 9 show that realistic boundaries and the Indian subcontinent do not have a prominent impact on equatorial currents and sea level for either the 180- and 90-day basin resonances; however, they do cause significant asymmetries about the equator near the eastern, western, and northern boundaries.

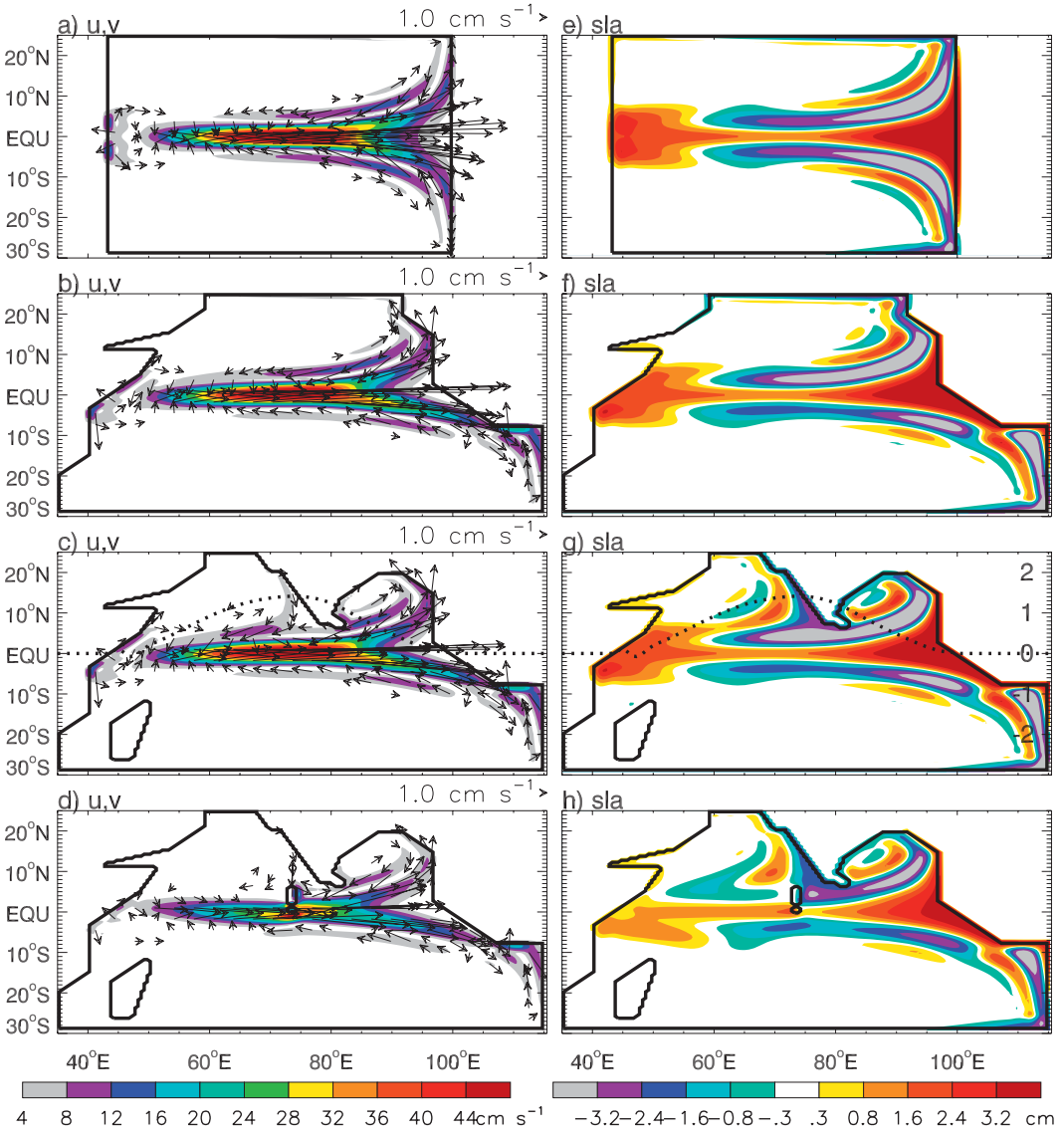

FIG. 8. Zonal and meridional surface currents u and v (cm s^{-1}; arrows) and their amplitudes (color contours) for the 180-day basin resonance when equatorial zonal surface current obtains its maximum amplitude (black line on Fig. 7d) from (a) LMExp3; (b) LMExp5; (c) LMExp6; and (d) LMExp7 (see Table 2). (e)–(h) The corresponding SLA (cm) are shown. The dotted black curve in (c) and (g) shows $-h_{yy}$ [cm (°)$^{-2}$], the negative of sea level curvature along the equator.

The Indian subcontinent and Sri Lanka, which extend into the tropics, allow the equatorial resonances to have a direct influence on sea level variations along the west coast of India, in addition to an indirect effect from the equator through the radiation of coastal Kelvin waves around the perimeter of the Bay of Bengal (cf. Figs. 8e–g). When sea level variations associated with the basin resonances in the central equatorial basin contact the Indian subcontinent and Sri Lanka, they propagate around Sri Lanka and then northward along the west coast of India as coastal Kelvin waves north of their critical latitudes (e.g., McCreary 1980) and westward-radiating Rossby waves south of their critical latitudes (see sea level structures of Figs. 8g, 9g).

The Maldives Islands weaken the 180- (Figs. 8d,h) and 120-day (not shown) resonance amplitudes. They do not, however, have an apparent impact on the 90-day basin resonance because they are located in a "node" region of the resonance (cf. Figs. 9c,d with Figs. 9g,h). Note that the Maldives are included as vertical walls, even at the surface; as such, their effect on the basin resonances in the model might be artificially stronger than they should be.

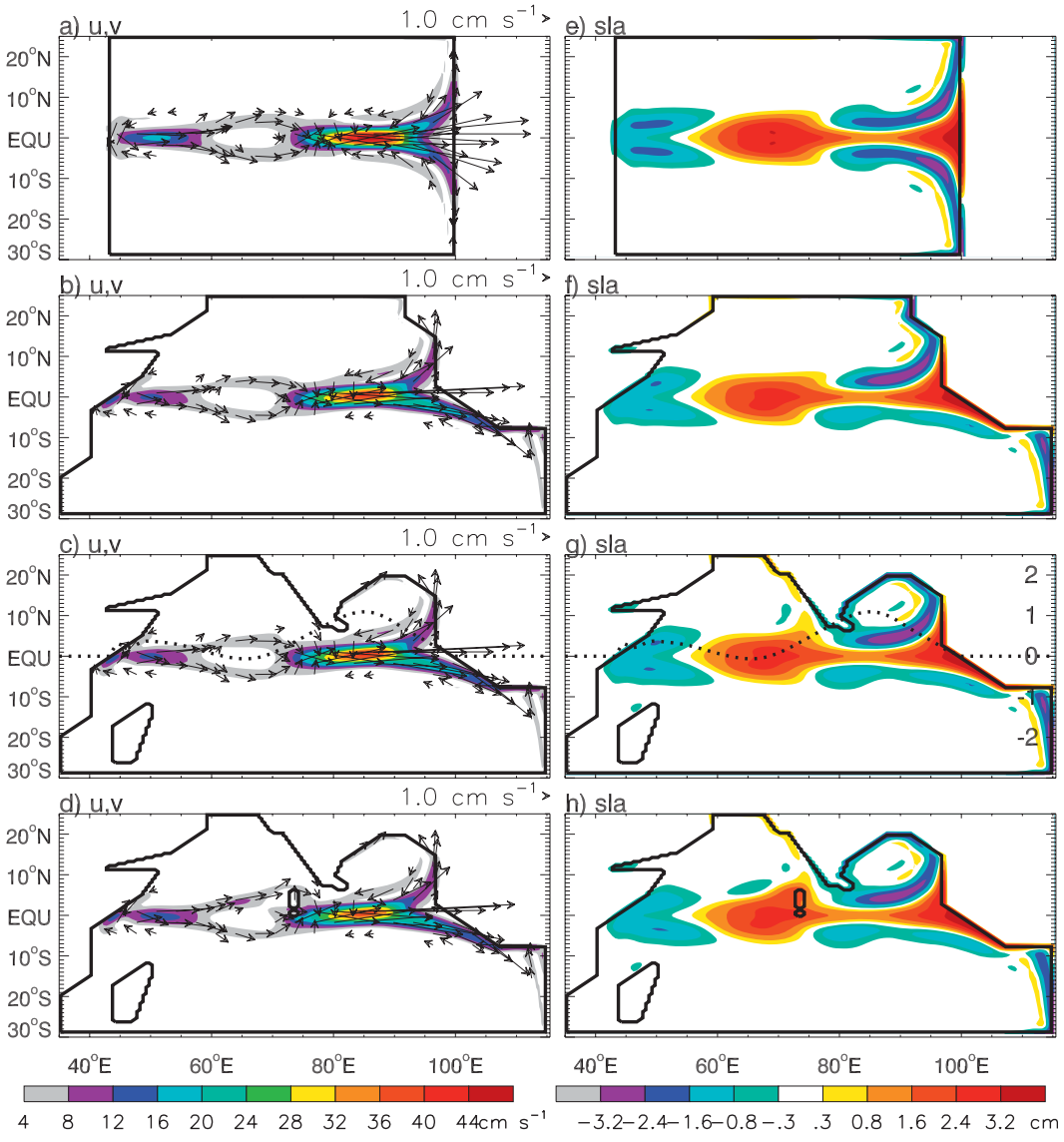

FIG. 9. As in Fig. 8, but for the 90-day basin resonance.

c. Key time scale to set up the basin resonances

Given that real IO winds are not purely sinusoidal, an important issue is how long it takes each basin resonance to become established. To address this issue, Figs. 11–13 show the transient response of IO surface currents and sea level to 180- and 90-day forcing by τ^x during year 1 of solution LMExp6. Comparisons of Figs. 11–13 with the basin-resonance structures in Figs. 7–9 suggest that the structures and amplitudes of both the 180- and 90-day resonances appear after day 180. For example, on day 45 of Fig. 12, currents and sea level mainly exhibit a Kelvin wave–like structure. By day 135, both Kelvin and $\ell = 1$ Rossby wave structures are evident, with large amplitudes of sea level appearing in the eastern equatorial basin and on both sides of the equator with an opposite sign. The relative maximum of sea level in the western equatorial basin for the 180-day basin resonance (Fig. 8g), however, is not yet established (Fig. 12e), and current amplitudes are still increasing (Figs. 11a, 12a–c). On day 225, the basin-resonance structures of both sea level and currents are set up (cf. Figs. 12c,f with Figs. 8c,g).

A similar development also occurs for the 90-day basin resonance, except that the transition to a basin-resonant structure near day 180 is even clearer. The double-maxima structure of zonal currents along the equator is not set up on either day 84 or 129 (Figs. 11b, 13); it begins to appear on day 171, after the westward-propagating $\ell = 1$ Rossby wave arrives at the western

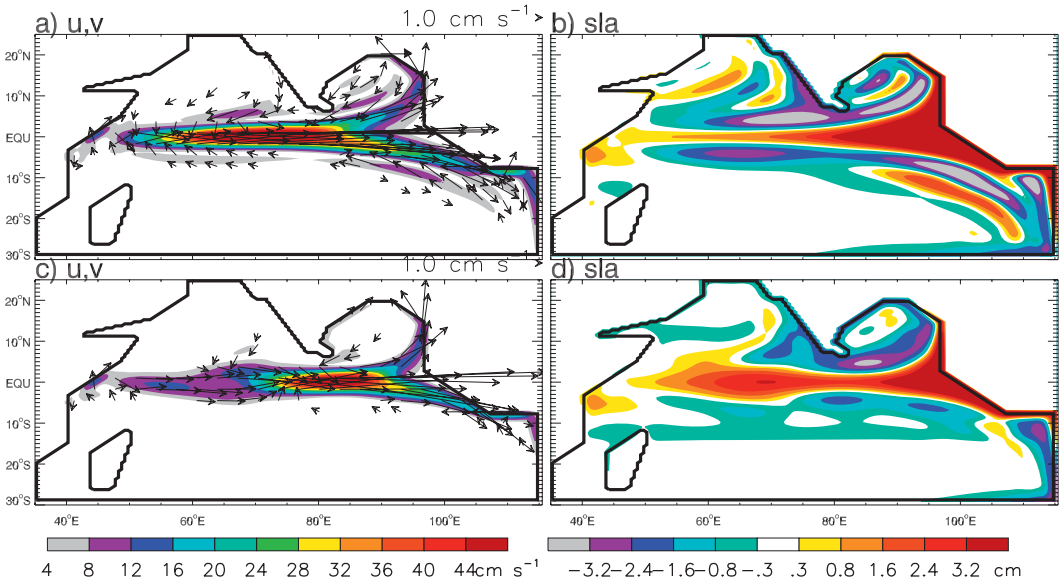

FIG. 10. (a),(b) As in Figs. 8c,g, but for the sum of $n = 1$ and $n = 2$ baroclinic modes surface currents and sea level at the 180-day period; (c),(d) As in (a),(b), but for the 90-day period; they are as in Figs. 9c,g, except for the sum of the $n = 1$ and $n = 2$ modes.

boundary, together with the sea level structure for the 90-day resonance (Fig. 9). The structures are even better developed on day 216 (cf. Figs. 13c,d,g,h with Figs. 9c,g).

Is the western boundary necessary for the existence of the current maximum in the eastern equatorial basin? Even though the transient processes suggest that the eastern maximum is primarily associated with direct wind forcing and eastern-boundary reflections, the amplitude of the eastern maximum still increases and the secondary maximum is set up in the western basin only after the western boundary is felt by the Rossby wave (cf. Figs. 13c,d). As shown for the 1D model, the equatorial IO will not selectively respond to the 180- and 90-day wind forcing without the western boundary.

These transient processes demonstrate that the time it takes to establish basin resonances is the time it takes a Kelvin wave to cross the basin and an $\ell = 1$ Rossby wave to return, the basic adjustment time scale of the equatorial ocean. Multiple reflections of these waves from basin boundaries are not needed. For the 180- and 90-day resonance of the $n = 2$ mode, this time is

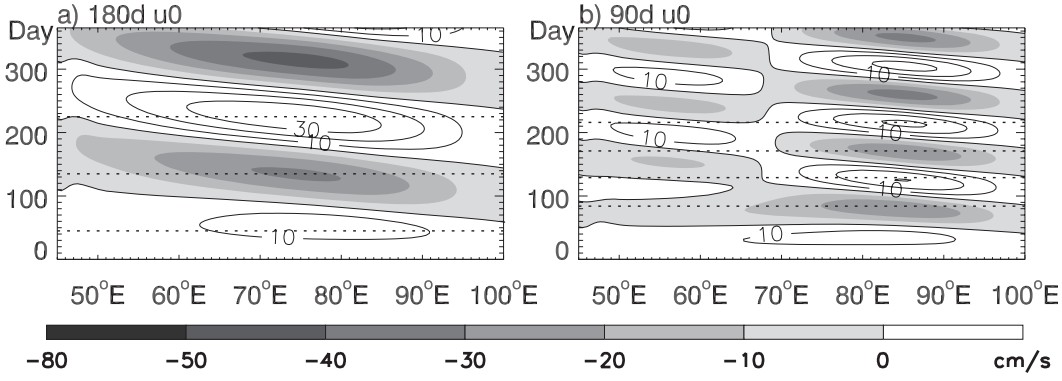

FIG. 11. (a) Longitude–time plots of zonal surface currents along the IO equator (2°S–2°N) for the $n = 2$ mode at 180-day period from the year-1 response of LMExp6, which illustrates transient processes for establishing the 180-day basin resonance. (b) As in (a), but for 90-day period. The black horizontal lines in (a) mark days 45, 135, and 225, and those in (b) mark days 84, 129, 171, and 216; they are the approximate times when the zonal surface currents of the basin resonances attain maximum amplitudes. Positive values are contoured and negative values are shaded, with an interval of 10 cm s^{-1}.

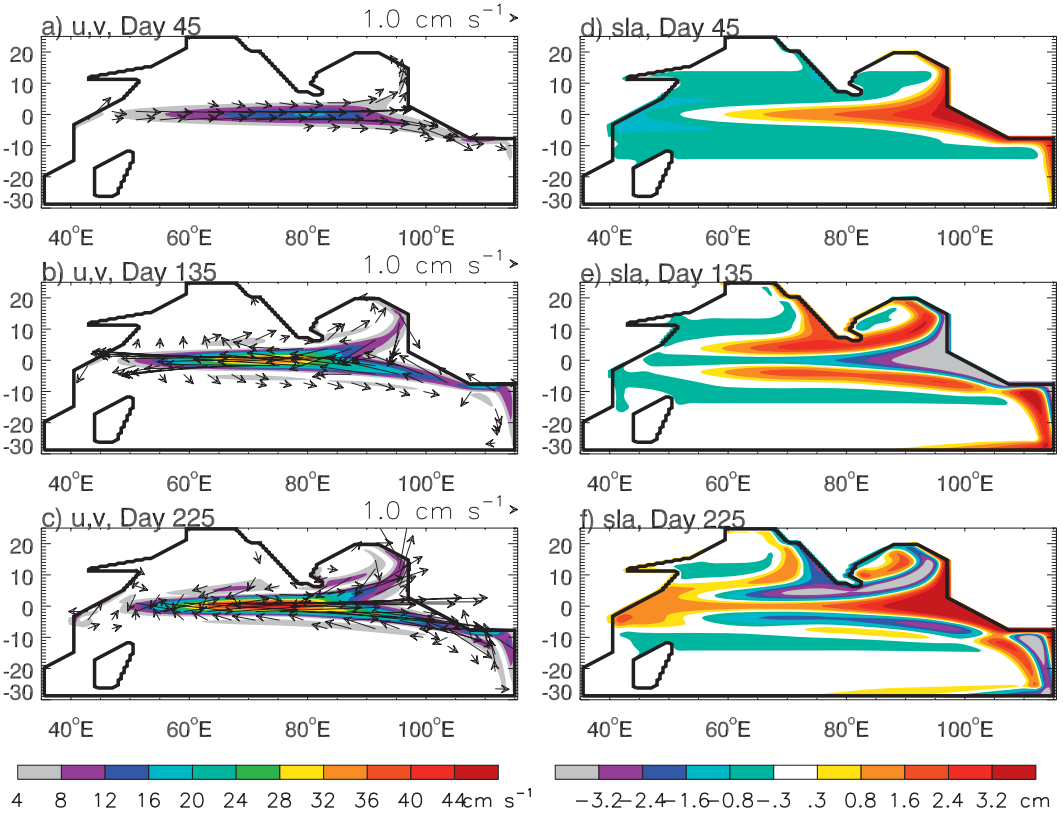

FIG. 12. (a)–(c) Zonal and meridional surface currents u and v (arrows; cm s^{-1}) and their amplitudes (color contours) for the 180-day basin resonance on days 45, 135, and 225 (dotted lines of Fig. 11a), the times when the equatorial zonal surface currents obtain their maximum amplitudes. (d)–(f) As in (a)–(c), but for SLA (cm).

approximately 180 days. For the 120-day resonance of the $n = 1$ mode, it is approximately 120 days.

d. Frequent excitation of the 90-day resonance in the real IO

Because the semiannual zonal winds are rather persistent along the IO equator, since they are associated with the seasonal monsoon transitions, it is expected that the 180-day basin resonance can be regularly excited. Given that the 90-day equatorial zonal wind has considerable seasonal-to-interannual variability (Han et al. 2006), is the 90-day basin resonance also frequently excited? To answer this question, we obtained an additional set of LCSM experiments to test the transient response of the equatorial IO to variable, 90-day winds. For example, when the 90-day forcing changes from being strong in the first half of the year to weak during the second half or vice versa, basin resonance is still established. On the other hand, if the wind blows for half a year and then is zero for the second half, current and sea level variations will diminish markedly and the 90-day basin resonance does not set up.

In the real IO, although the equatorial zonal winds have significant power near 90 days, their spectral peak at intraseasonal time scales occurs in the 30–60-day band (Fig. 14a) associated with the Madden–Julian oscillation (MJO; e.g., Madden and Julian 1971, 1972). Will the ocean still have larger response near the 90-day period than at 30–60-day periods? To answer this question, we obtained a solution to HYCOM in a realistic IO basin forced by satellite-observed QuikSCAT winds (section 2c) and a corresponding LCSM solution forced by the same wind [linear model control run (LM_CR); Table 2]. Even though the winds are stronger at 30–60 days, the largest sea level response clearly is shifted to be near 90 days in both solutions, with the shift being more evident in the HYCOM solution (Figs. 14c,d). The preferred oceanic response near the 90-day period in the models is consistent with satellite sea level data (Fig. 14b), albeit with some quantitative differences. For example, the spectral peaks occur near 100 days in HYCOM but near 90 days in the observations (cf. Figs. 14b,d). This difference may be because bottom topography in HYCOM is smoothed by 10° × 10° boxes so that continental shelves near the equator may not be

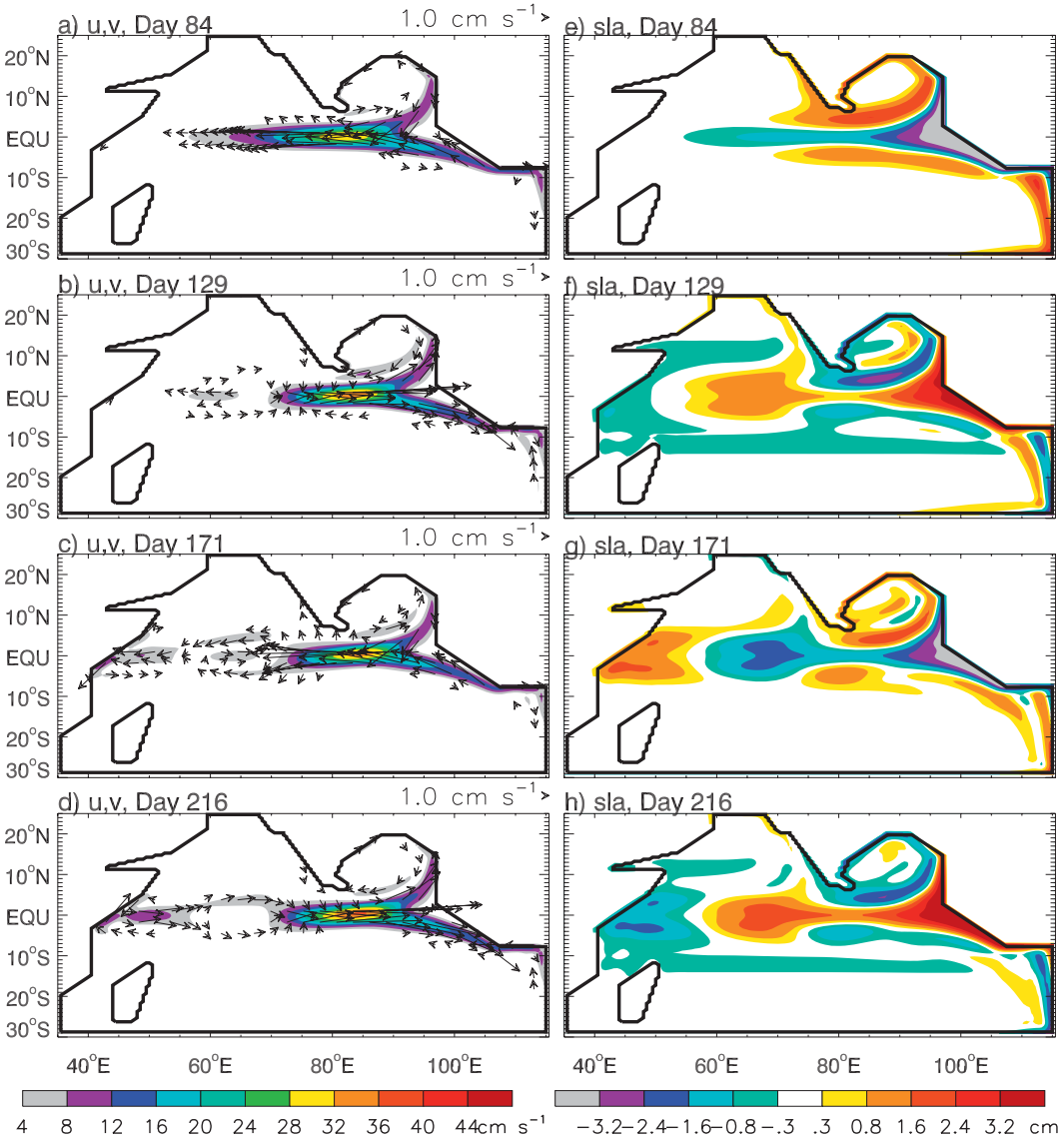

FIG. 13. As in Fig. 12, but for the 90-day basin resonance on days 84, 129, 171, and 216 (dotted lines of Fig. 11b), the times when the zonal surface current amplitudes attain their maxima.

accurately represented, thereby enlarging the zonal distance of the equatorial basin and lengthening the resonance period.

Note that the N^2 profile used to calculate the baroclinic mode speeds for the LCSM varies only with depth, which yields a constant mode speed for a given baroclinic mode (section 2b). In the HYCOM solution and real IO, N^2 changes spatially and hence so do the mode speeds (Doi et al. 2010). The fact that strong near 90-day response frequently occurs in the LCSM, HYCOM, and observations (Fig. 14) suggests that the 90-day basin resonance can be frequently excited in the equatorial IO, even though the forcing by the 90-day wind has considerable seasonal-to-interannual variability and the mode speeds vary spatially.

4. Summary and discussion

In this paper, we revisit the 180- and 90-day basin resonances that occur in the equatorial IO to clarify several unresolved issues: the causes for the eastern-basin concentration of the 90-day resonance, the time scale for their establishment, and the likelihood that the 90-day resonance is excited in the real IO. In addition, we investigate the 120-day basin resonance, examine the effects of IO basin geometry, and explore the phase

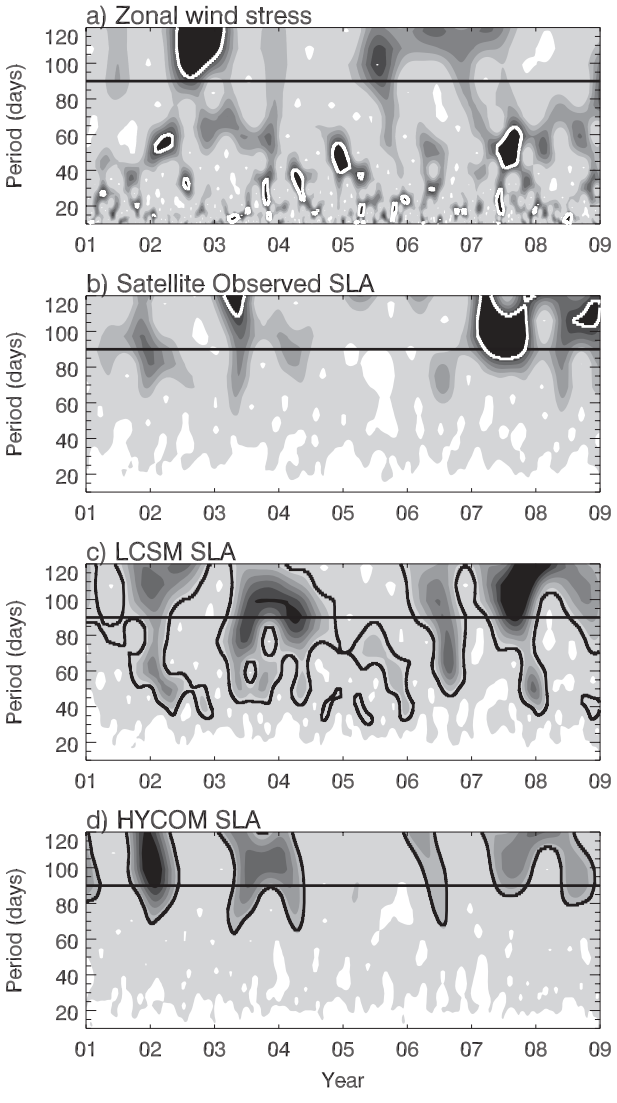

FIG. 14. a) The local, normalized wavelet power spectra (Torrence and Compo 1998) of 3-day mean QuikSCAT zonal wind stress averaged over the central equatorial basin (5°S–5°N, 60°–95°E) for the period of 2001–08. (b) As in (a), but for weekly AVISO satellite SLA averaged in the eastern equatorial basin (5°S–5°N, 80°–110°E). (c) As in (b), but for 3-day mean LCSM SLA. (d) As in (b), but for 3-day mean HYCOM SLA. Darker shading indicates higher power. The white/black contour-enclosed regions indicate where the significance of results exceeds the 95% confidence level.

propagation of zonal surface currents associated with the equatorial basin resonances. To achieve our goals, we obtain solutions to a hierarchy of models: an idealized 1D ocean model (section 2a; Table 1), a more realistic LCSM (section 2b; Table 2), and an OGCM (HYCOM; section 2c).

Consistent with theoretical predictions, the 180-day basin resonance has one zonal-current maximum in the central basin, and the 90-day basin resonance has two relative maxima of zonal-current in the eastern and western basin (Figs. 3, 4, 7–9). Both are associated with the second baroclinic mode ($n = 2$), and they are mainly forced by winds within the tropics (Figs. 5, 6). The corresponding sea level structures are more complex (Figs. 8, 9). These structures qualitatively agree with those observed 180- and 90-day zonal surface current and sea level in the equatorial basin (Fig. 1). Note that the observed 90-day sea level structure from Archiving, Validation, and Interpretation of Satellite Oceanographic data (AVISO) shows significant amplitude in the western equatorial basin (Fig. 1f), where very weak or no power is shown in previous studies (Han 2005; Fu 2007); this difference is likely because previous studies are based on Ocean Topography Experiment (TOPEX)/*Jason-1* single satellite data, which have much lower resolution in the equatorial region than the multisatellite merged AVISO product shown here.

Horizontal and vertical mixings are the major cause for the eastern-basin concentration of the 90-day zonal surface current and sea level, with contributions from other baroclinic modes further enhancing the eastern-basin maximum (Figs. 3–5, 8–10; section 3a). Mixing enhances the eastern-basin response, because the $\ell = 1$ Rossby wave propagates more slowly than the Kelvin wave and thus is more damped, thereby producing a larger amplitude in the eastern basin. This east–west asymmetry exists only when friction is added in the 1D model, and it results from asymmetries of both the directly forced response and boundary reflections (Figs. 3, 4). Zonal surface currents associated with the basin modes propagate westward along the equator faster than the speed of an $\ell = 1$ Rossby wave, a consequence of interference primarily between boundary Kelvin and Rossby waves, with a contribution from the wind-forced interior solution in some regions.

Without damping in the 1D model, the basin resonances become unrealistically large (Figs. 2, 3a–c, 4a–c). Without a western boundary, however, resonance does not occur and thus oceanic responses will not exhibit 90- and 180-day peaks when the model is forced by white noise (Fig. 2). By contrast, in 3D models, energy leaks into higher latitudes, where it is damped by horizontal mixing so that even without vertical mixing solutions remain finite (Figs. 5, 8, 9). In addition, we also found a basin resonance at 120 days associated with the $n = 1$ mode. The peak at the 120-day period in mode-1 solution, however, is not detectable when all baroclinic modes or even the first two baroclinic modes are summed if the forcing is white noise (Fig. 5c). Consequently, we expect that this basin resonance will be visible in the real ocean and OGCM solutions only if the 120-day winds have a significant peak.

The time it takes the Kelvin wave to cross the basin and $\ell = 1$ Rossby wave to return is the time scale for the setup of all basin resonances. It is approximately 180 days for the 180- and 90-day basin resonances (Figs. 11–13) and about 120 days for the 120-day basin resonance. Multiple reflections of waves from basin boundaries are not needed to establish basin resonances. In the real IO, then, the 180- and 90-day basin resonances can be frequently excited (section 3d; Fig. 14), even though a few factors can impede their establishment, such as nonlinearity, changes of mode speeds associated with spatial change in stratification, and large temporal variability of the 90-day wind field. Contrary to the above, Sengupta et al. (2007) argued that 90 days is the intrinsic time scale for equatorial IO adjustment and hence that neither periodic wind forcing at 90 days nor oceanic resonance is required to account for enhanced 90-day oceanic variability. It seems to us, however, that their transient model experiments (upon which their conclusions were based) indicate an adjustment time scale closer to 180 days (see their Fig. 10), in which case their explanation for the prevalence of 90-day variability does not follow.

The Indian subcontinent (including Sri Lanka), which extends southward to about 8°N, is a major cause for the north–south asymmetry about the equator, enabling a strong and direct influence of the equatorial resonances on sea level variability along the west coast of India (Figs. 8, 9). The Maldives Islands appear to weaken the 180-day basin resonance, but they have little influence on the 90-day resonance because they fall into the ''node'' region between the two relative current maxima.

Note that our 1D and LCSM solutions are forced by winds without eastward propagation. This may be true for the semiannual zonal winds, which are associated with basinwide summer/winter monsoon transitions. At the 90-day period, however, part of its power may be associated with MJO-like variability, which propagates eastward at a speed of 5–10 m s^{-1} over the IO. Han et al. (2001) examined the eastward-moving winds on resonances, finding that they acted to strengthen the eastward Kelvin wave and to weaken the westward Rossby wave but did not eliminate the resonance.

Finally, attention should be paid when interpreting the observed and OGCM-simulated sea level and currents; they consist of contributions from all baroclinic modes, which can obscure the basin resonance structures associated with a single baroclinic mode (cf. Figs. 1, 8–10). Consequently, bandpassing fields to focus on a specific resonant period band may not isolate the pure basin-resonant structure, even though the observed structures might be dominated by basin resonances in the equatorial region. Note also that resonance only explains the relative peaks at the 180- and 90-day periods (Fig. 2). It cannot explain all the power at these periods, because other baroclinic modes and directly forced waves can also have significant contributions (Figs. 2, 5c, 7, 10).

Acknowledgments. We wish to express our appreciation to Dr. Peter Gent at NCAR for reading through the manuscript and providing corrections. We also thank Dr. Lee-Lueng Fu for his helpful comments and discussions. The NCEP air temperature and specific humidity and CMAP precipitation data are provided by the NOAA/OAR/ESRL PSD, Boulder, Colorado, from their Web site (at http://www.esrl.noaa.gov/psd/). QuikSCAT wind data are produced by Remote Sensing Systems and sponsored by the NASA Ocean Vector Winds Science Team. Data are downloaded from http://www.remss.com. The altimeter products were produced by Ssalto/Duacs and distributed by AVISO, with support from CNES (http://www.aviso.oceanobs.com/duacs/). We thank Dr. Yuanchong Zhang for providing the ISCCP flux data. Weiqing Han and Benet Duncan are supported by NASA Ocean Surface Topography Science Team Program Award NNX08AR62G, NSF CAREER Award OCE 0847605 and NASA Ocean Vector Wind Science Team Program Award 1283568. Julian P. McCreary is supported by the Japan Agency for Marine–Earth Science and Technology (JAMSTEC) through its sponsorship of the International Pacific Research Center (IPRC).

REFERENCES

Anderson, D. L. T., and D. J. Carrington, 1993: Modeling interannual variability in the Indian Ocean using momentum fluxes from the operational weather analyses of the United Kingdom Meteorological Office and European Centre for Medium Range Weather Forecasts. *J. Geophys. Res.,* **98,** 12 483–12 499.

Bentamy, A., K. B. Katsaros, W. M. Drennan, and E. B. Forde, 2002: Daily surface wind fields produced by merged satellite data. *Gas Transfer at Water Surfaces, Geophys. Monogr.,* Vol. 127, Amer. Geophys. Union, 343–349.

Bleck, R., 2002: An oceanic general circulation model framed in hybrid isopycnic-Cartesian coordinates. *Ocean Modell.,* **4,** 55–88.

Bonjean, F., and G. S. E. Lagerloef, 2002: Diagnostic model and analysis of the surface currents in the tropical Pacific Ocean. *J. Phys. Oceanogr.,* **32,** 2938–2954.

Cane, M. A., and D. W. Moore, 1981: A note on low frequency equatorial basin modes. *J. Phys. Oceanogr.,* **11,** 1578–1584.

——, and E. S. Sarachik, 1981: The response of a linear baroclinic equatorial ocean to periodic forcing. *J. Mar. Res.,* **39,** 651–693.

Doi, T., T. Tozuka, and T. Yamagata, 2010: Equivalent forcing depth in tropical oceans. *Dyn. Atmos. Oceans,* **50,** 415–423.

Donguy, J. R., and G. Meyers, 1995: Observations of geostrophic transport variability in the western tropical Indian Ocean. *Deep-Sea Res.,* **42,** 1007–1028.

Ducet, N., P.-Y. Le Traon, and G. Reverdin, 2000: Global high resolution mapping of ocean circulation from TOPEX/Poseidon and ERS-1/2. *J. Geophys. Res.,* **105,** 19 477–19 498.

Fu, L.-L., 2007: Intraseasonal variability of the equatorial Indian Ocean observed from sea surface height, wind, and temperature data. *J. Phys. Oceanogr.,* **37,** 188–202.

Gent, P. R., 1981: Forced standing equatorial ocean wave modes. *J. Mar. Res.,* **39,** 695–709.

——, K. O'Neill, and M. A. Cane, 1983: A model of the semiannual oscillation in the equatorial Indian Ocean. *J. Phys. Oceanogr.,* **13,** 2148–2160.

Gill, A. E., 1982: *Atmosphere–Ocean Dynamics*. Academic Press, 662 pp.

Halliwell, G. R., 1998: Simulation of North Atlantic decadal/multidecadal winter SST anomalies driven by basin-scale atmospheric circulation anomalies. *J. Phys. Oceanogr.,* **28,** 5–21.

——, 2004: Evaluation of vertical coordinate and vertical mixing algorithms in the Hybrid Coordinate Ocean Model (HYCOM). *Ocean Modell.,* **7,** 285–322.

Han, W., 2005: Origins and dynamics of the 90-day and 30–60-day variations in the equatorial Indian Ocean. *J. Phys. Oceanogr.,* **35,** 708–728.

——, J. P. McCreary, D. L. T. Anderson, and A. J. Mariano, 1999: Dynamics of the eastward surface jets in the equatorial Indian Ocean. *J. Phys. Oceanogr.,* **29,** 2191–2209.

——, D. M. Lawrence, and P. J. Webster, 2001: Dynamical response of equatorial Indian Ocean to intraseasonal winds: Zonal flow. *Geophys. Res. Lett.,* **28,** 4215–4218.

——, P. J. Webster, R. Lukas, P. Hacker, and A. Hu, 2004: Impact of atmospheric intraseasonal variability in the Indian Ocean: Low-frequency rectification in equatorial surface current and transport. *J. Phys. Oceanogr.,* **34,** 1350–1372.

——, T. Shinoda, L. Fu, and J. P. McCreary, 2006: Impact of atmospheric intraseasonal oscillations on the Indian Ocean dipole during the 1990s. *J. Phys. Oceanogr.,* **36,** 670–690.

Iskandar, I., W. Mardiansyah, Y. Masumoto, and T. Yamagata, 2005: Intraseasonal Kelvin waves along the southern coast of Sumatra and Java. *J. Geophys. Res.,* **110,** C04013, doi:10.1029/2004JC002508.

——, T. Tozuka, H. Sasaki, Y. Masumoto, and T. Yamagata, 2006: Intraseasonal variations of surface and subsurface currents off Java as simulated in a high-resolution ocean general circulation model. *J. Geophys. Res.,* **111,** C12015, doi:10.1029/2006JC003486.

Jensen, T. G., 1993: Equatorial variability and resonance in a wind-driven Indian Ocean model. *J. Geophys. Res.,* **98** (C12), 22 533–22 552.

Jerlov, N. G., 1976: *Marine Optics*. Elsevier, 231 pp.

Kalnay, E., and Coauthors, 1996: The NCEP/NCAR 40-Year Reanalysis Project. *Bull. Amer. Meteor. Soc.,* **77,** 437–471.

Knox, R. A., 1976: On a long series of measurements of Indian Ocean equatorial currents near Addu Atoll. *Deep-Sea Res.,* **23,** 211–221.

Large, W. G., J. C. McWilliams, and S. C. Doney, 1994: Oceanic vertical mixing: A review and a model with a nonlocal boundary layer parameterization. *Rev. Geophys.,* **32,** 363–403.

——, G. Danabasoglu, S. C. Doney, and J. C. McWilliams, 1997: Sensitivity to surface forcing and boundary layer mixing in a global ocean model: Annual-mean climatology. *J. Phys. Oceanogr.,* **27,** 2418–2447.

Levitus, S., and T. P. Boyer, 1994: *Temperature*. Vol. 4, *World Ocean Atlas 1994,* NOAA Atlas NESDIS 4, 117 pp.

——, R. Burgett, and T. P. Boyer, 1994: *Salinity*. Vol. 3, *World Ocean Atlas 1994,* NOAA Atlas NESDIS 3, 99 pp.

Luyten, J. R., and D. H. Roemmich, 1982: Equatorial currents at semi-annual period in the Indian Ocean. *J. Phys. Oceanogr.,* **12,** 406–413.

Madden, R. A., and P. R. Julian, 1971: Detection of a 40–50 day oscillation in the zonal wind of the tropical Pacific. *J. Atmos. Sci.,* **28,** 702–708.

——, and ——, 1972: Description of global-scale circulation cells in the tropics with a 40–50 day period. *J. Atmos. Sci.,* **29,** 1109–1123.

McCreary, J. P., 1980: Modeling wind-driven ocean circulation. Hawaii Institute of Geophysics Tech. Rep. HIG-80-3, 64 pp.

——, 1981: A linear stratified ocean model of the coastal undercurrent. *Philos. Trans. Roy. Soc. London,* **302A,** 385–413.

——, W. Han, D. Shankar, and S. R. Shetye, 1996: On the dynamics of the East India Coastal Current 2: Numerical solutions. *J. Geophys. Res.,* **101,** 13 993–14 010.

McPhaden, M. J., 1982: Variability in the central equatorial Indian Ocean. Part 1: Ocean dynamics. *J. Mar. Res.,* **40,** 157–176.

Miyama, T., J. McCreary, T. Jensen, J. Loschnigg, S. Godfrey, and A. Ishida, 2003: Structure and dynamics of the Indian-Ocean cross-equatorial cell. *Deep-Sea Res. II,* **50,** 2023–2047.

Molinari, R. L., D. Olson, and G. Reverdin, 1990: Surface current distributions in the tropical Indian Ocean derived from compilations of surface buoy trajectories. *J. Geophys. Res.,* **95,** 7217–7238.

Moore, D. W., and J. P. McCreary, 1990: Excitation of intermediate-frequency equatorial waves at a western ocean boundary: With application to observations from the Indian Ocean. *J. Geophys. Res.,* **95,** 5219–5231.

Nagura, M., and M. J. McPhaden, 2010: Wyrtki Jet dynamics: seasonal variability. *J. Geophys. Res.,* **115,** C07009, doi:10.1029/2009JC005922.

O'Brien, J. J., and H. E. Hurlburt, 1974: An equatorial jet in the Indian Ocean, theory. *Science,* **184,** 1075–1077.

Qiu, B., M. Mao, and Y. Kashino, 1999: Intraseasonal variability in the Indo–Pacific Throughflow and the regions surrounding the Indonesian Seas. *J. Phys. Oceanogr.,* **29,** 1599–1618.

Reppin, J., F. A. Schott, J. Fischer, and D. Quadfasel, 1999: Equatorial currents and transports in the upper central Indian Ocean: Annual cycle and interannual variability. *J. Geophys. Res.,* **104,** 15 495–15 514.

Sengupta, D., R. Senan, B. N. Goswami, and J. Vialard, 2007: Intraseasonal variability of equatorial Indian Ocean zonal currents. *J. Climate,* **20,** 3036–3055.

Shankar, D., J. P. McCreary, W. Han, and S. R. Shetye, 1996: On the dynamics of the East India Coastal Current, Part 1: Analytic solutions forced by interior Ekman pumping and local alongshore winds. *J. Geophys. Res.,* **101** (C6), 13 975–13 991.

Tang, W., and W. T. Liu, 1996: Objective interpolation of scatterometer winds. Jet Propulsion Laboratory Publication 19, 16 pp.

Torrence, C., and G. P. Compo, 1998: A practical guide to wavelet analysis. *Bull. Amer. Meteor. Soc.,* **79,** 61–78.

Wyrtki, K., 1973: An equatorial jet in the Indian Ocean. *Science,* **181,** 262–264.

Xie, P., and P. A. Arkin, 1996: Analyses of global monthly precipitation using gauge observations, satellite estimates, and numerical model predictions. *J. Climate,* **9,** 840–858.

Yuan, D., and W. Han, 2006: Roles of equatorial waves and western boundary reflection in the seasonal circulation of the equatorial Indian Ocean. *J. Phys. Oceanogr.,* **36,** 930–944.

Zhang, Y., W. B. Rossow, A. A. Lacis, V. Oinas, and M. I. Mishchenko, 2004: Calculation of radiative fluxes from the surface to top of atmosphere based on ISCCP and other global data sets: Refinements of the radiative transfer model and the input data. *J. Geophys. Res.,* **109,** D19105, doi:10.1029/2003JD004457.